A cyclostationary multi-domain analysis of fluid instability in Kaplan turbines

P. Pennacchi [a]*, P. Borghesani [b1], S. Chatterton [a2]

* Corresponding author.Tel.: +39 0223998440, E-mail address: paolo.pennacchi@polimi.it (P. Pennacchi)

[a] Politecnico di Milano, Dipartimento di Meccanica, Via la Masa 1, 20156 Milano (MI), Italy

[b] School of Chemistry, Physics and Mechanical Engineering, Queensland University of Technology, Brisbane, QLD 4001, Australia

http://dx.doi.org/10.1016/j.ymssp.2014.08.026

Abstract

Hydraulic instabilities represent a critical problem for Francis and Kaplan turbines, reducing their useful life due to increase of fatigue on the components and cavitation phenomena. Whereas an exhaustive list of publications on computational fluid-dynamic models of hydraulic instability is available, the possibility of applying diagnostic techniques based on vibration measurements has not been investigated sufficiently, also because the appropriate sensors seldom equip hydro turbine units. The aim of this study is to fill this knowledge gap and to exploit fully, for this purpose, the potentiality of combining cyclostationary analysis tools, able to describe complex dynamics such as those of fluid-structure interactions, with order tracking procedures, allowing domain transformations and consequently the separation of synchronous and non-synchronous components. This paper will focus on experimental data obtained on a full-scale Kaplan turbine unit, operating in a real power plant, tackling the issues of adapting such diagnostic tools for the analysis of hydraulic instabilities and proposing techniques and methodologies for a highly automated condition monitoring system.

Keywords

Hydraulic instability; condition monitoring; cyclostationarity; order tracking; rotatordynamics; Kaplan turbine.

1. Introduction

The detection of hydraulic instabilities in Francis and Kaplan turbines for power generation is a key issue to avoid drastic reductions of the turbine life. High vibrations may arise in the shaft as a consequence of those abnormal pressure fluctuations in the flow, in turn causing fatigue problems on the turbine components, as shown by Presas *et al.* [1], Egusquiza *et al.* [2]. Moreover, cavitation problems are also associated with such phenomena (see for instance Ausoni *et al.* [3], Escaler *et al.* [4]), resulting in a faster degradation of the surfaces of the runner.

Hydraulic instabilities have been studied in the past mainly by means of computational fluid-dynamics (CFD) models and pressure measurements within the flow in prototype turbines. The first

[1] Tel.: +61 0401531045, E-mail address: p.borghesani@qut.edu.au (P. Borghesani)
[2] Tel: +39 0223998442, E-mail address: steven.chatterton@polimi.it (S. Chatterton)

mentioning of vortex instabilities in a close conduct is likely due to Kelvin in 1910 [5]. His study, despite neglecting significant factors such as turbulence and viscosity, remained substantially the state of the art until the '60. Only then, the studies by Hoffman and Joubert [6] and Kreith and Sonju [7], proved, with experimental tests, that their turbulence models could be introduced in the description of vortexes in a pipe. Despite the fact that investigation of flow in hydraulic turbines was considered a significant issue, as demonstrated by the experimental investigations on turbine prototypes by Wigle *et al.* [8], Hosoi [9] and Kolyachev and Lasenko [10], no major breakthrough was made in this application until Ruprecht et al. [11][12] finally introduced in the first years of the this century the full dynamics of a 3-dimensional unsteady turbulent flow in the simulation of a Francis turbine, including the rotor and stator interactions. Later studies, as those by Susan-Resiga *et al.* [13], Zhang *et al.* [14] and Liu *et al.* [15], focused particularly on vortex rope instability, which was described as an unsteady motion of vortices in the draft tube of Francis turbines, often happening in partial load conditions. Fluid-dynamical studies on Kaplan turbines are also available in the literature, such as that by Wang *et al.* [16], focusing on experimental measurement of the flow, and Liu *et al.* [17][18][19], implementing CFD models for the prediction of pressure fluctuations, further verified by means of a turbine prototype.

The possibility to exploit vibrations to detect and investigate the nature of such phenomena has not been analysed before previous preliminary works by the authors on this topic [20][21]. In those papers, order tracking techniques were applied to isolate the non-synchronous part of the vibration signal and therefore highlight the harmonics which characterized the hydraulic instability in a Kaplan turbine. The preliminary investigations reported in those papers were however limited to simple first order cyclostationary indicators, like the Short Time Fourier Transform and its order domain counterpart, similarly to what is usually employed in the few studies available in the literature for Francis turbine, such as Bajic and Keller [22] and Escaler *et al.* [23]. In this way, it was possible to characterize the phenomenon only in relation to its periodic/deterministic behaviour, while all the information carried in the random part was neglected.

As shown by Antoni [24], second order cyclostationary components are often significant, or even dominant, in the dynamics of many rotating and reciprocating mechanical systems, including fluid machines such as compressors and internal combustion motors. The concepts of cyclostationary analysis were brought from the field of telecommunications to mechanical engineering thanks to the works of Randall *et al.* [25] and further developed by Antoni *et al*. [26][27]. The basic idea of cyclostationarity is to look into periodicities of the statistical properties of the signal [28], mainly mean (first order cyclostationarity) and variance (second order cyclostationarity). While the first order tools are substantially coincident with the traditional Fourier analysis ones, the second are able to provide information on signals which have interactions between periodic and random components. In particular, second order cyclostationary tools have proven their effectiveness in describing modulations of random carriers by deterministic components and non-exactly periodic phenomena.

Despite the absence, to the best of the authors' knowledge of any study regarding cyclostationary tools applied to hydraulic turbines, the coupling of unstable and ergodic phenomena, characteristic of turbulent flows, and macroscopic cyclic behaviours, typical of fluid structure interactions, suggest the potential of such techniques for this application.

Therefore, the aims of this paper are:

1. to further detail and describe the application of first order cyclostationary tools for the detection of fluid instabilities, including the necessary domain transformations;

2. to investigate the nature of the hydrodynamic instability by means of second order cyclostationary analysis, providing a further tool for the diagnostics of hydraulic turbines.

This study will take advantage of experimental measurements on a real Kaplan turbine unit installed in an Italian power plant. The sketch of the turbine is shown in Figure 1.

Figure 1 about here

2. The Kaplan turbine

The turbine unit under investigation is shown in Figure 2. It consists of a 7 blades runner, able to process a 91 m^3/s flow with nominal speed of 166.67 rpm (2.778 Hz), net head of 27,95 m and a maximum power output of 23.388 MW. The turbine is connected to a 18 poles synchronous generator, thus obtaining the European standard electric frequency of 50 Hz.

Figure 2 about here

2.1. Finite element model

A finite element model (FEM) of the shaft, based on beam elements, has been programmed, as described in the previous work [20], to obtain an estimate of the natural frequencies and eigenmodes of the shaft for the lateral vibrations. Some model data are reported in annex A. A sketch of the shaft-line model is reported in Figure 3.

Figure 3 about here

The first two modes, relative to the runner, are shown in the Figure 4 and Figure 5, corresponding respectively to natural frequencies of 6.00 Hz and 15.52 Hz for backward modes, 6.17 Hz and 19.54 Hz for forward modes.

Figure 4 about here

Figure 5 about here

2.2. Measurement setup

The turbine unit is equipped with a series of sensors, including for vibration measurements:

- Two couple of Brüel & Kjær Vibro IN-081 proximitors measuring lateral rotor vibrations in two orthogonal directions. The sensors were installed in two different measuring planes, in correspondence of the unit bearings (turbine journal bearing - Brg. #1 and generator journal bearing Brg. #2 in Figure 3).
- One Brüel & Kjær Vibro IN-081 proximitor measuring axial vibrations.
- An additional Brüel & Kjær Vibro IN-081 proximitor acting as a key-phasor to provide a tachometer measurement.

Vibration measurements were acquired at the sampling rate of 500 Hz by a National Instruments SCXI 1000 chassis and 4 boards SCXI 1305, with embedded anti-aliasing filters, along with other unit operating parameters, like the rotational speed, the active power, etc.

In this paper, only the results for the Brg. #1 measuring plane measurements are reported for the sake of brevity. Similar results have been obtained also for Brg. #2.

3. Experimental test

The experimental test analysed in this paper consists of a plant start-up, which allows investigating different operating conditions and their effect on hydraulic instability.

The start-up of the plant consists of three phases: first the rotational speed is brought gradually to the nominal value of 2.778 Hz (corresponding to an electric frequency of 50 Hz, due to the 18 poles pairs). Then the unit is connected to the grid (synchronization) and, finally, the load applied by the generator is gradually increased to obtain the desired power output.

Figure 6 reports an example of such procedure, including the final moments of the speed ramp and the first part of the load increase. In particular, diagram (a) shows an estimate of the instantaneous electric frequency of the generator, obtained by processing the signal of a 1x rev. tachometer installed on the shaft (a 18X multiplication factor was introduced to convert the shaft speed in the electric frequency). Diagram (b) shows the instantaneous power output of the generator, obtained by means of electric measurements, and directly proportional to the load (torque) applied on the shaft. Note that the spikes at about 55 s correspond to the grid synchronization. Diagram (c) shows the vibrations measured in two orthogonal directions of Brg. #1 measuring plane by two proximitors installed on the stator. All signals have been sampled with a sampling rate of 500 Hz.

Figure 6 about here

It is possible to notice a macroscopic increase of vibrations, at the operational speed, when the load is kept in the range 3-5 MW. This is also evident if rotor orbits are considered: Figure 6 (d) shows the direct and 1X rotor orbits at about 3 MW, while (e) at about 16 MW, moreover it also evident that the vibration harmonic content is very different in the two load conditions of Figure 6 (d) and (e).

By calculating a simple spectrogram of the two signals measured by the proximity probes, it is possible to obtain some insight on the dynamics of such vibrations. Figure 7 was obtained by applying a short time Fourier transform (STFT), based on 10 second long Hamming windows, with a 5 second overlap among two adjacent windows. Both diagrams are dominated by the series of harmonics of the shaft rotational speed, which are always present and stabilize soon on the nominal frequency of 2.778 Hz (corresponding to 50 Hz of electric frequency). However, in the time range between 100 and 300 s, three strong additional components arise. Moreover, overall noise levels increase in this time frame, suggesting a not fully harmonic phenomenon, as it also rather evident from Figure 6 (d), where direct rotor orbit is unquestionably not closed.

Figure 7 about here

In the following sections the phenomenon will be investigated by means of advanced order tracking and cyclostationary tools.

3.1. Order tracking

The first step to clarify the behaviour of the machine is to remove the synchronous components, which are present also during the normal functioning of the turbine, and are therefore not useful for diagnostic purposes of instabilities. This can be done by applying computed order tracking (COT),

followed by a synchronous averaging (SA), and finally subtract the average behaviour from the signal.

COT is a technique [29] is a family of techniques aimed at obtaining a uniform angular sampling by means of interpolations on a uniformly time sampled signal, *i.e.* transforming a measured signal $x[n\Delta t]$ in the estimated signal $\hat{x}[m\Delta\theta]$ where $\Delta\theta$ is a fixed (small) angular rotation of a reference shaft.

A simple algorithm implementing the COT, based on linear interpolations and a 1x revolution keyphasor is explained as follows. The tacho signal $\xi[n\Delta t]$ is measured on a reference shaft, providing a 1x revolution reference:

$$\xi[n\Delta t] = \begin{matrix} 0 \text{ if } 0 + 2\pi k \le \theta(n\Delta t) < \alpha + 2\pi k \\ 1 \text{ if } \alpha + 2\pi k \le \theta(n\Delta t) < 2\pi(k+1) \end{matrix} \quad \text{with } 0 < \alpha < 2\pi \text{ and k} = 0, \dots, \text{K} \tag{1}$$

A simple edge detecting algorithm is used on the tacho signal to identify the time instants corresponding to complete revolutions of the shaft (angles $\alpha + 2\pi k$):

$$t_k = (n_k + 0.5)\Delta t \quad \text{with} \quad \xi[n_k\Delta t] = 0 \quad \text{and} \quad \xi[(n_k+1)\Delta t] = 1 \tag{2}$$

Then an estimation of the angles $\theta[n\Delta t]$ corresponding to each sample of $x[n\Delta t]$ is obtained (disregarding the constant arbitrary phase shift α) by means of a first (piecewise linear) interpolation:

$$\hat{\theta}[n\Delta t] = 2\pi\left(k + \frac{n\Delta t - t_k}{t_{k+1} - t_k}\right) \quad \text{with } t_k \le n\Delta t < t_{k+1} \tag{3}$$

Once the desired number of samples M per revolution is chosen, a second interpolation will finally lead to the estimation of the uniformly angular sampled signal $\hat{x}[m\Delta\theta]$:

$$\hat{x}[m\Delta\theta] = x[n\Delta t] + \frac{m\Delta\theta - \hat{\theta}[n\Delta t]}{\hat{\theta}[(n+1)\Delta t] - \hat{\theta}[n\Delta t]}\,(x[(n+1)\Delta t] - x[n\Delta t]) \tag{4}$$

$$\text{with } \hat{\theta}[n\Delta t] \le m\Delta\theta < \hat{\theta}[(n+1)\Delta t] \quad \text{and} \quad \Delta\theta = 2\pi/M$$

The so obtained signal will have MP samples, *i.e.* M samples per each of the P revolutions. This constant number of samples per revolution allows the application of the SA, consisting in the calculation of the average one-revolution behaviour of $\hat{x}[m\Delta\theta]$:

$$\hat{x}_{SA}[m\Delta\theta] = \sum_{p=0}^{P-1} \hat{x}[(m + pM)\Delta\theta] \quad \text{with } m = 0{:}\, M-1 \tag{5}$$

This synchronous average component can be removed from the original signal to find the so called residual:

$$\hat{x}_r[m\Delta\theta] = \hat{x}[m\Delta\theta] - \hat{x}_{SA}\left[\left(m - \left\lfloor\frac{m}{M}\right\rfloor M\right)\Delta\theta\right] \tag{6}$$

with $\lfloor\cdot\rfloor$ indicating a rounding down operation.

A series of issues have to be tackled in order to ensure a good result of the SA procedure.

- It is necessary to isolate a time window in which the components to be removed keep stable in amplitude. Therefore, it has been chosen to analyse two sections of the vibration signals separately: a first part (hereafter called subrecord A see Figure 6) from 100 s to 300 s, where the speed is constant and the load on the turbine is low (~3.3 MW). A second part (hereafter called subrecord B) from 500 s to 700 s at the same constant speed but with a high load (~15 MW).
- A sufficiently precise tacho signal should be selected for this purpose. Noticing the speed fluctuations of Figure 6 (a), probably not feasible in such a high inertia rotor, and considering that the tacho gives a only a 1x revolution reference, the tacho signal is not considered as reliable for this purpose. Therefore, it may result more effective to use the Improved Synchronous Averaging (ISA) [30][31] technique, taking advantage of the strong high frequency harmonics of the shaft within the vibration signal itself. This technique will extract an artificial tacho signal from the vibration signal itself, by narrow band-pass filtering the vibration signal around a multiple of the shaft speed.
- The uncertain nature of the non-synchronous components suggests keeping their study in the frequency domain, instead than in the order one. Therefore it will be necessary to transform the signal back to time domain (using the same artificial tacho signal), after having removed the synchronous component in the angular domain of the shaft. To do this, an approach already suggested by the authors in the past [32], though not yet implemented, is applied and explained later.

The ISA technique isolates a harmonic of the vibration signal itself by narrow band-pass filtering and uses it as a tacho signal:

$$\xi[n\Delta t] = x[n\Delta t] \otimes w_{f_c,\Delta f}[n\Delta t] \tag{7}$$

where $w_{f_c,\Delta f}[n\Delta t]$ is a band pass filter with central frequency f_c and bandwidth Δf and $\otimes$ is the convolution operator. f_c is set according to the average speed of the shaft ω_{avg} and the target multiple M, while the bandwidth is chosen accordingly to the expected speed fluctuation $\Delta\omega$ and considering Carson's rule for frequency modulated signals. If possible (depending on the presence of strong multiples and the width of $\Delta\omega$) a high order multiple $M\omega_{avg}$ is chosen, in order to obtain a high resolution tacho-equivalent signal (*i.e.* with many edges per revolution), able to track small changes of speed within one revolution of the shaft.

Figure 8 shows the digital ideal filtering applied to the *x*-vibration signal, which is defined as a narrow band of 2.778 Hz, centred on the 27th harmonic (75 Hz). The 27th harmonic has been chosen for its

high order, leading to a high precision in following speed variations, and for its high amplitude (strong signal to noise ratio).

Figure 8 about here

The resulting inversed Fourier transformed signal is then used as a normal tachometer signal to perform COT. This procedure is repeated for the two subrecords A and B of the signal, obtaining the improvements shown in Figure 9. Only *x*-vibrations will be shown here for the sake of brevity, the same steps are applied with similar results to *y*-direction vibrations.

Figure 9 about here

The spectrograms of the residuals now show clearly the different behaviour of the two signals, with no significant component in subrecord B, Figure 9 (d) and the three non-synchronous components of subrecord A, Figure 9 (c).

However, as said before, to better identify the nature of these components it is suitable to return to the frequency domain. The process used is based on an Ariadne's thread approach: an artificially generated signal is subjected to the same order tracking operation as the vibration subrecord and, after having cleaned the vibration signal in the order domain, it is used as a reference to invert the transformation back to the starting point of the time domain.

The reference signal is generated in time domain, with a length equal to the one of the subrecord under analysis. In particular this reference signal has been arbitrarily chosen as a 10 Hz sinewave. This signal is order-tracked using the same tachometer signal described in Figure 8, in parallel to the vibration signals. When the signals of Figure 9 (c) and (d) have been obtained, the order-tracked reference sinewave, now distorted in the transformation to the order domain, is used as a tachometer signal to operate a second COT operation, in this case from the angular to the time domain. This procedure is displayed in Figure 10.

Figure 10 about here

The results for both directions of vibration are shown in Figure 11 for the subrecord A and Figure 12 for the subrecord B. The location of the anomalous peaks is now possible with accuracy by comparing the two cases.

Figure 11 about here

Figure 12 about here

In particular it is possible to identify the following frequency components which are present only at low load (subrecord A):

- 0.3 Hz component, dominating the spectrum, not very stable.
- 6 Hz component, corresponding to the first bending mode of the shaft.
- 15.5 Hz component, corresponding to the second bending mode of the shaft.

It is also possible to notice, especially in *x* direction vibrations, a couple of sidebands of the 1st harmonics of the shaft, exactly spaced from the nominal 2.778 Hz frequency by an interval of 0.3 Hz,

indicating a coupling of this phenomenon with the 1x revolution vibrations of the shaft. All this 1st order cyclostationary (periodic) components are typical of an instability.

However, given the strong unstable behaviour of such fluid-structure interactions, it is natural to also expect components with higher orders of cyclostationarity, whose presence is suggested also by high overall noise levels for the overall duration of subrecord A.

3.2. Second order cyclostationary analysis

A first attempt to look into the second order cyclostationary (CS2) content of the signal consists in calculating the STFT of the envelope of a high pass filtered version of the vibration signal. The choice of a high pass is dictated by the need of removing the 1st order cyclostationary components listed at the end of previous section and still present in the signal. Half of the Nyquist frequency has been chosen as cut-off frequency for the ideal digital filter applied to the time domain residual signals of the two subrecords (output of the procedure of Figure 10).

The result of the envelope analysis is reported in Figure 13 for subrecord A and in Figure 14 for subrecord B.

Figure 13 about here

Figure 14 about here

While for the second subrecord the only CS2 harmonics are the ones of the rotational speed, subrecord A shows clear CS2 components at 9.5 Hz, 12 Hz, 21.5 Hz and 31 Hz. These components can be easily explained as modulating effects of the natural frequencies of the system on random hydraulic phenomena. Being the natural vibrations sinusoidal and given the squaring operator involved in the envelope operation, the peaks corresponding to resonances will have their frequency doubled in cyclic domain, thus resulting in the 12 Hz (2×6 Hz) and 31 Hz (2×15.5 Hz). The other two peaks at 9.5 and 12.5 are nothing but the combinations of the two resonances (15.5±6 Hz).

To prove the validity of such considerations a simple numerical signal $x(t)$ has been generated. It is composed by white noise amplitude modulated by a biharmonic signal as follows.

$$x(t) = \left[sin\left(6 \cdot 2\pi t + \frac{\pi}{12}\right) + sin\left(15.5 \cdot 2\pi t + \frac{\pi}{12}\right)\right] \cdot w(t) \tag{8}$$

where $w(t)$ is white noise (pseudo standard normal random series).

The sampling frequency has been set to 500 Hz and a 10 s record of the signal has been generated (see Figure 15).

Figure 15 about here

Then the envelope spectrum of this signal has been obtained applying the same filtering used for the Kaplan turbine signal (upper half band pass). The result of the envelope spectrum, shown in Figure 16 is exactly matching the peak pattern of the Kaplan case.

Figure 16 about here

3.1. Detailing the CS2 components in the envelope spectrum

Once the key CS2 components have been identified, information can be obtained on the characteristics of the fluid-dynamic phenomenon by means of more sophisticated CS2 analysis tools: the cyclic correlation (or averaged cyclic periodogram) and the cyclic coherence.

The two indicators are described in detail by Antoni [27] and allow identifying both the macroscopic cyclic frequencies of a CS2 signal and their corresponding spectral support, i.e. in case of deterministic/random modulation, associate to each deterministic modulating component found in the envelope spectrum, the spectral characterization of its random carrier.

The cyclic correlation $S_x(f,\alpha)$ is basically defined as the expected value of the autocorrelation of the spectrum itself:

$$S_x(f,\alpha) = \boldsymbol{E}\left\{X\left(f+\frac{\alpha}{2}\right)\cdot X^*\left(f-\frac{\alpha}{2}\right)\right\} \tag{9}$$

and it is estimated by means of the averaged cyclic periodogram as described in [27].

This two dimensional indicator identifies simultaneously the power associated with the frequency f, in a traditional spectral sense, and varying (modulation) at a cyclic frequency α, from the CS2 (envelope) point of view.

The cyclic coherence $\gamma_x(f,\alpha)$ is the normalized version of the cyclic correlation, defined as:

$$\gamma_x(f,\alpha) = \frac{S_x(f,\alpha)}{\sqrt{\left|S_x\left(f+\frac{\alpha}{2}\right)\right|\left|S_x\left(f-\frac{\alpha}{2}\right)\right|}} \tag{10}$$

Given the computational effort required to obtain such indexes on large cyclic frequency ranges, it has been chosen to split the analysis concentrating singularly on each component of the envelope spectrum. Moreover, given the similarities of the two measurement direction, only the *x*-direction will be reported for the sake of brevity.

The first component identified in the envelope spectrum is located at 9.5 Hz, resulting from the difference of the two natural frequencies of the turbine. The spectral correlation, calculated on a cyclic neighbourhood of 9.5 Hz is shown in Figure 17 (a). It is possible to notice that the energy associated with the 9.5 Hz cyclic component has a wide spectral support. The overall decreasing level of energy, moving towards the higher spectral frequencies, may mislead the consideration on the spectral characterization of this component.

Figure 17 about here

More normalized information is given by the spectral coherence, which provides an indication of the share of the total energy at the frequency f associated with the cyclic frequency α. As shown in Figure 17 (b), the coherence grows significantly towards higher spectral bands, indicating a higher importance of the modulating phenomenon in that area. This can be explained by the fact that, at such frequency, no external disturbance can be found and the hydraulic instability effect dominates the signal.

The same considerations apply for the other three cyclic components (12, 21.5 and 31 Hz).

3.2. Kurtosis as a synthetic CS2 diagnostic tool

In order to automate the detection of such problem in the CS2 indicator, a very simple, compact and non-dimensional measure of the CS2 content of a signal can be obtained by the time domain kurtosis of the band-pass filtered analytic signal (henceforth simply kurtosis) used for the calculation of the envelope. As explained in a previous work [33], thanks to the Parseval's theorem it is possible to demonstrate that the kurtosis is nothing but the sum of all the peaks of the squared envelope spectrum, normalized by the zero-frequency peak. High kurtosis values mean that the envelope spectrum is non-flat and possess high non-zero frequency peaks.

In the experimental cases of Figure 13 and Figure 14, the kurtoses are respectively:

- 4.5 in *x* direction and 4.6 in *y* direction for subrecord A (hydraulic instability)
- 4.0 in *x* direction and 3.5 in *y* direction for subrecord B (normal operation)

The small difference of kurtosis between the two conditions is due to the presence of the synchronous peaks in the envelope spectrum of subrecord B, which keep the kurtosis high despite the absence of the peaks due to the hydraulic instability. The presence of the peaks can be due to the imperfection of the order tracking operations or really connected to some effect of the rotating speed on hydro-dynamics. However, if not solved, it compromises any attempt to develop any automated system for the detection of hydraulic problems based on kurtosis.

A possible solution resides in applying SA to the envelope signal: as done for the raw signal, it is possible to obtain the SA of the envelope signal and subtract it from the envelope itself, obtaining a residual envelope signal, whose synchronous components have been removed. This operation is included in the process of Figure 10, which is modified in the form of Figure 18.

Figure 18 about here

The results of this procedure are shown in Figure 19 and Figure 20, respectively for subrecord A and B. It is evident that, whereas no significant change happens for the hydraulic instability case, subrecord B shows a significant decrease in the amplitude of the CS2 shaft harmonics.

Figure 19 about here

Figure 20 about here

Once the envelope spectrum has been cleaned, it is easy to calculate a far more reliable kurtosis, as:

$$\kappa_x = \frac{\sum |ES[k]|^2}{|ES[0]|^2} \tag{11}$$

This results in a far more reliable kurtosis:

- 4.3 in *x* direction and 4.4 in *y* direction for subrecord A (hydraulic instability)
- 2.2 in *x* direction and 2.1 in *y* direction for subrecord B (normal operation)

As for the envelope spectra, the SA operation did not affect significantly subrecord A, which shows a dominance of non-shaft related CS2 peaks. On the contrary, for subrecord B (normal conditions) the kurtosis returns very near the theoretical value of 2, which is expected in case of no significant CS2 component.

4. Conclusions

In this paper, a detailed analysis of the vibrating phenomena caused by vortex rope instability in a Kaplan turbine has been provided. Step-by-step diagnostic procedures involving domain transformations and 1st and 2nd order cyclostationary indicators have been illustrated, showing their effectiveness in detecting the insurgency of this problem. Moreover, a synthetic kurtosis-based indicator has been derived, in order to allow programming simple but reliable automated condition monitoring systems. Being the first attempt to apply cyclostationary analysis to fluid-dynamic phenomena, this paper represents a starting point for future works in this field. Future steps will necessarily involve improved measurement setups, able to widen the frequency range under investigation and allowing comparisons between vibration signals and flow measurements.

References

[1] A. Presas, C. Valero, X. Huang, E. Egusquiza, M. Farhat, F. Avellan, Analysis of the dynamic response of pump-turbine runners-Part I: Experiment, IOP Conference Series: Earth and Environmental Science 15 (PART 5), art. no. 052015, pp. 1-8.

[2] E. Egusquiza, C. Valero, X. Huang, E. Jou, A. Guardo, C. Rodriguez, Failure investigation of a large pump-turbine runner, Engineering Failure Analysis, 23 (2012), pp. 27-34.

[3] Ph. Ausoni, M. Farhat, X. Escaler, E, Egusquiza, F. Avellan, Cavitation Influence on von Kármán Vortex Shedding and Induced Hydrofoil Vibrations, Journal of Fluids Engineering, 129 August (2007), pp. 966-973.

[4] X. Escaler, M. Farhat, E. Egusquiza, F. Avellan, Dynamics and Intensity of Erosive Partial Cavitation, Journal of Fluids Engineering, 129 July (2007), pp. 886-893.

[5] W.T. Kelvin, Vibrations of a Columnar Vortex, Mathematical and Physical Papers, Cambridge University Press, Vol. IV (1910), Chapter 15, 152-165.

[6] E.R. Hoffman, P.N. Joubert, Turbolent line vortices, Journal of Fluid Mechanics, 16(3) (1963), 395-411.

[7] F. Kreith, O.K. Sonju, The decay of a turbulent swirl in a pipe, Journal of Fluid Mechanics, 22(2) (1965), pp. 257-271.

[8] D.A. Wigle, et al., Hydraulic Model Studies for Turbines at Grand Coulee Powerplant, (1946) Hydraulic Laboratory Report No. Hyd.198, U.S. Bureau of Reclamation, Denver, CO, USA.

[9] Y. Hosoi, Experimental investigations of pressure surge in draft tubes of Francis water turbines, Hitachi Review, 14(12) (1965).

[10] V.A. Kolychev, V.E. Lasenko, Issledovanie potoka v radial' no-osevoi gidroturbine (Investigation of Flow in Francis Hydraulic Turbines), (1966) Izvestiya Vysshikh Vchebnykh Zavedenii (Moskeva) Energetika, 2, pp. 89-96.

[11] A. Ruprecht, M. Heitele, and M. Helmrich, Numerical Simulation of a Complete Francis Turbine Including Unsteady Rotor/Stator Interactions, in: Proc. 20th IAHR Symposium on Hydraulic Machinery and Systems (2000), Charlotte, NC, pp. 1-8.

[12] A. Ruprecht, T. Helmrich, T. Aschenbrenner, T. Scherer, Simulation of vortex rope in a turbine draft tube, in: Proc. 21st IAHR Symposium on Hydraulic Machinery and Systems (2002), 9–12 September, Lausanne, Switzerland, pp. 1-8.

[13] R. Susan-Resiga, G.D.Ciocan, I. Anton, F. Avellan, Analysis of the swirling flow downstream a Francis turbine runner, ASME Journal of Fluids Engineering, 128(1) (2006), pp. 177-189.

[14] R.K. Zhang, F. Mao, J.Z. Wu, S.Y. Chen, Y.L. Wu, S.H. Liu, Characteristic and control of the draft-tube flow in part-load Francis turbine, ASME Journal of Fluids Engineering, 131(2) (2009), pp. 021101 (13 pages).

[15] S.H. Liu, L. Zhang, M. Nishi, Y.L. Wu, Cavitating turbulent flow simulation in a Francis turbine based on mixture model, ASME Journal of Fluids Engineering, 131(5) (2009), pp. 053102 (8 pages).

[16] Z.W. Wang, L. Quin, J.D. Zeng, J.Y. Lin, J.Y. Yang, W.J. Chen, Y.Y. Luo, Z.G. Yan, Hydroturbine operating region partitioning based on analyses of unsteady flow field and dynamic response, Science China Technological Sciences, 53(2) (2010), pp. 519-528.

[17] S.H. Liu, J. Shao, S.F. Wu, Y.L. Wu, Numerical simulation of pressure fluctuation in Kaplan turbine, Science in China Series E: Technological Sciences, 51(8) (2008), pp. 1137-1148.

[18] S.H. Liu, S.C. Li, Y.L Wu., Pressure fluctuation prediction of a model Kaplan turbine by unsteady turbulent flow simulation, ASME Journal of Fluids Engineering, 131(10) (2009), pp. 101102 (9 pages).

[19] S. Liu, D. Zhou, D. Liu, Y. Wu, M. Nishi, Runaway transient simulation of a model Kaplan turbine, Proc. 25th IAHR Symposium on Hydraulic Machinery and Systems, September 20–24, 2010, Timişoara, Romania, pp. 1-8.

[20] P. Pennacchi, A. Vania, S. Chatterton, E. Tanzi, Detection of unsteady flow in a Kaplan hydraulic turbine using machine mechanical model and rotor measured vibrations, Proceedings of ASME Turbo Expo 2012, June 11-15, 2012, Copenhagen, Denmark, paper GT20102-69995, pp. 1-10.

[21] P. Pennacchi, P. Borghesani, S. Chatterton, A. Vania, Hydraulic Instability Onset Detection in Kaplan Turbines by Monitoring Shaft Vibrations, in Proceedings of ASME 24th Conference on Mechanical Vibration and Noise (2012), pp. 715-722.

[22] B. Bajic, A. Keller, Spectrum normalization method in vibro-acoustical diagnostic measurements of hydroturbine cavitation, Journal of Fluids Engineering, 118 (1996), pp. 756-761.

[23] X. Escaler, E. Egusquiza, M. Farhat, F. Avellan, M. Coussirat, Detection of cavitation in hydraulic turbines, Mechanical Systems and Signal Processing, 20 (2006), pp. 983-1007.

[24] J. Antoni, Cyclostationarity by examples, Mech. Syst. Signal Process. 23.4 (2009), 987-1036.

[25] R. B. Randall, J. Antoni, S. Chobsaard, The relationship between spectral correlation and envelope analysis in the diagnostics of bearing faults and other cyclostationary machine signals, Mech. Syst. .Signal Process. 15(5) (2001), 945-962.

[26] J. Antoni, *et al*. Cyclostationary modelling of rotating machine vibration signals, Mech. Syst. Signal Process. 18(6) (2004), 1285-1314.

[27] J. Antoni, Cyclic spectral analysis of rolling-element bearing signals: Facts and fictions, Journal of Sound and vibration 304(3) (2007), 497-529.

[28] A.V. Dandawate, G.B. Giannakis, Statistical tests for presence of cyclostationarity, Signal Processing, IEEE Transactions on 42.9 (1994): 2355-2369.

[29] K.R. Fyfe, E.D.S. Munck, Analysis of computed order tracking, Mech. Syst. Signal Process. 11 (2) (1997) 187–205.
[30] M.D. Coats, N. Sawalhi, R.B. Randall. Extraction of tach information from a vibration signal for improved synchronous averaging, in: Proceedings of Acoustics, 2009, Adelaide (Australia), 23-25 November 2009.
[31] P. Borghesani, P. Pennacchi, R.B. Randall, R. Ricci, Order tracking for discrete-random separation in variable speed conditions, Mech. Syst. Signal Process. 30 (2012) 1–22.
[32] P. Borghesani, R. Ricci, S. Chatterton, P. Pennacchi, A new procedure for using envelope analysis for rolling element bearing diagnostics in variable operating conditions, Mech. Syst. Signal Process. 38 (2013) 23–35.
[33] P. Borghesani, P. Pennacchi, S. Chatterton, The relationship between kurtosis- and envelope-based indexes for the diagnostic of rolling element bearings, Mech. Syst. Signal Process. 43 (2014) 25–43.

Annex A – Kaplan turbine model data

The Kaplan turbine model, shown in Figure 3, is made of 54 beam elements with 7 rigid disks, in correspondence of the runner, generator poles, fan and exciter.

Bearing dynamic coefficients, provided by bearings' manufacturer, are:

- Turbine journal bearing: stiffness 9.221e+008 N/m, damping 1.368e+007 Ns/m
- Generator journal bearing: stiffness 2.392e+008 N/m, damping 4.918e+006 Ns/m

The supporting structure is considered as rigid.

Figure captions

Figure 1. Sketch of the Kaplan turbine.

Figure 2. Kaplan turbine unit after installation.

Figure 3. Sketch of the FEM.

Figure 4. First bending mode affecting the runner: (a) backward mode with natural frequency of 6.0 Hz, (b) forward mode at 6.2 Hz.

Figure 5. Second bending mode affecting the runner: (a) backward mode with natural frequency of 15.5 Hz, (b) forward mode at 19.5 Hz.

Figure 6. Measurements during start-up: (a) electric instantaneous frequency, obtained by processing a tachometer signal: (b) instantaneous power output, (c) rotor vibrations in two orthogonal directions of the shaft section, measured by proximitors installed in the stator at the turbine end of the shaft, (d) rotor direct and 1X orbits at about 3MW, (e) rotor direct and 1X orbits at about 16MW.

Figure 7. Raw spectrograms of the vibration signals: (a) *x* direction; (b) *y* direction. All diagrams have log scale z axis.

Figure 8. Extraction of an artificial tacho signal from the vibration signal itself (*x* vibration) by band pass filtering in the spectral domain.

Figure 9. Removal of synchronous components in the *x-vibration* signal: (a) spectrogram of the subrecord A before order tracking, (b) spectrogram of subrecord B before order tracking, (c) spectrogram of the residual of subrecord A after COT/SA, (d) spectrogram of the residual of subrecord B after COT/SA. All diagrams have log scale z axis.

Figure 10. Procedure to obtain clean vibration signals in time domain, without additional experimental signals.

Figure 11. Residual of the subrecord A: (a) spectrogram *x* direction; (b) spectrogram *y* direction; (c) spectrum *x* direction; (d) spectrum *y* direction. All diagrams have log scale z axis.

Figure 12. Residual of the subrecord B: (a) spectrogram *x* direction; (b) spectrogram *y* direction; (c) spectrum *x* direction; (d) spectrum *y* direction. All diagrams have log scale z axis.

Figure 13. Envelope analysis for the subrecord A: (a) envelope spectrogram *x* direction; (b) envelope spectrogram *y* direction; (c) envelope spectrum *x* direction; (d) envelope spectrum *y* direction. All diagrams in linear scale.

Figure 14. Envelope analysis for the subrecord B: (a) envelope spectrogram *x* direction; (b) envelope spectrogram *y* direction; (c) envelope spectrum *x* direction; (d) envelope spectrum *y* direction. All diagrams in linear scale.

Figure 15. First second of the artificially generated signal obtained modulating white noise with a biharmonic signal.

Figure 16. Envelope spectrum of the numerical simulation of a CS2 signal due to a biharmonic modulation of white noise.

Figure 17. Neighbourhood of 9.5 Hz, subrecord A: (a) cyclic correlation, Log z-axis scale

Figure 18. Procedure to obtain clean envelope signals in time domain, without additional experimental signals.

Figure 19. Envelope analysis for the subrecord A after removal of synchronous CS2 components: (a) envelope spectrogram *x* direction; (b) envelope spectrogram *y* direction; (c) envelope spectrum *x* direction; (d) envelope spectrum *y* direction.

Figure 20. Envelope analysis for the subrecord B after removal of synchronous CS2 components: (a) envelope spectrogram *x* direction; (b) envelope spectrogram *y* direction; (c) envelope spectrum *x* direction; (d) envelope spectrum *y* direction.

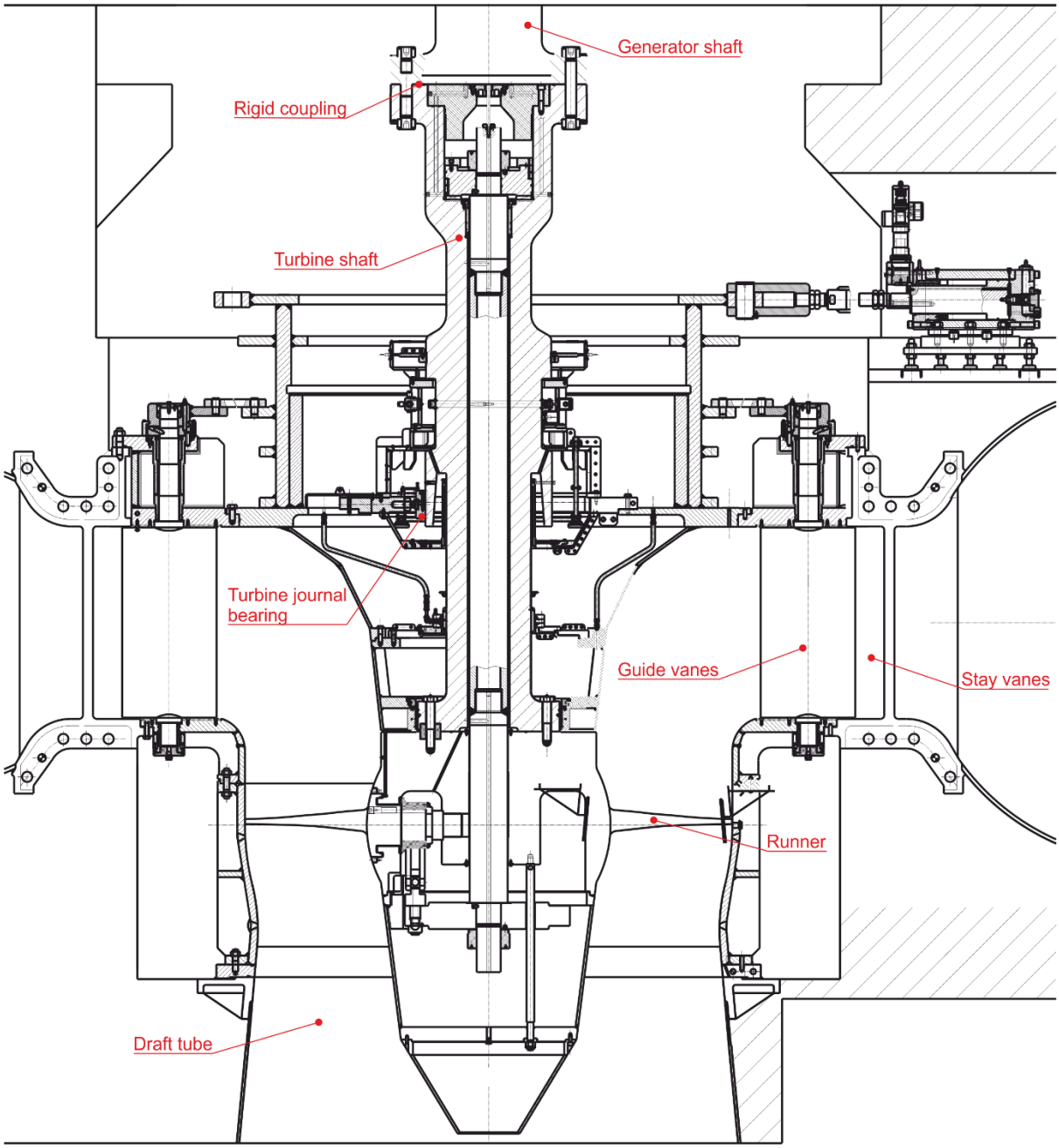

Figure 1. Sketch of the Kaplan turbine.

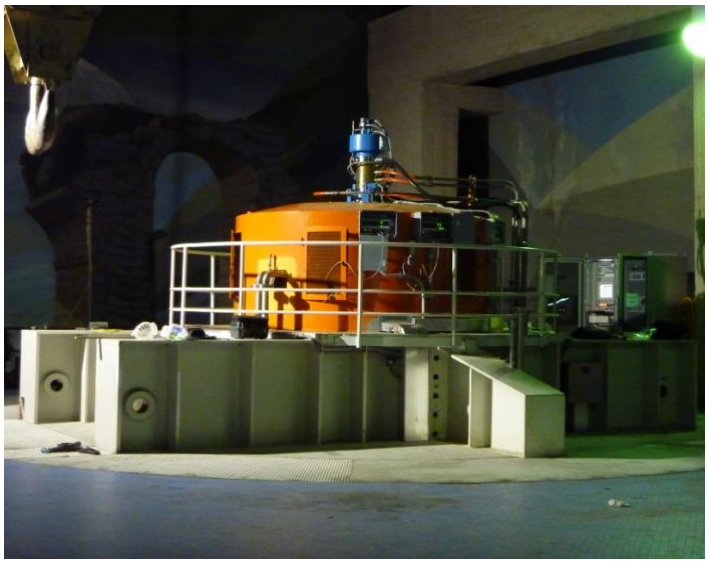

Figure 2. Kaplan turbine unit after installation.

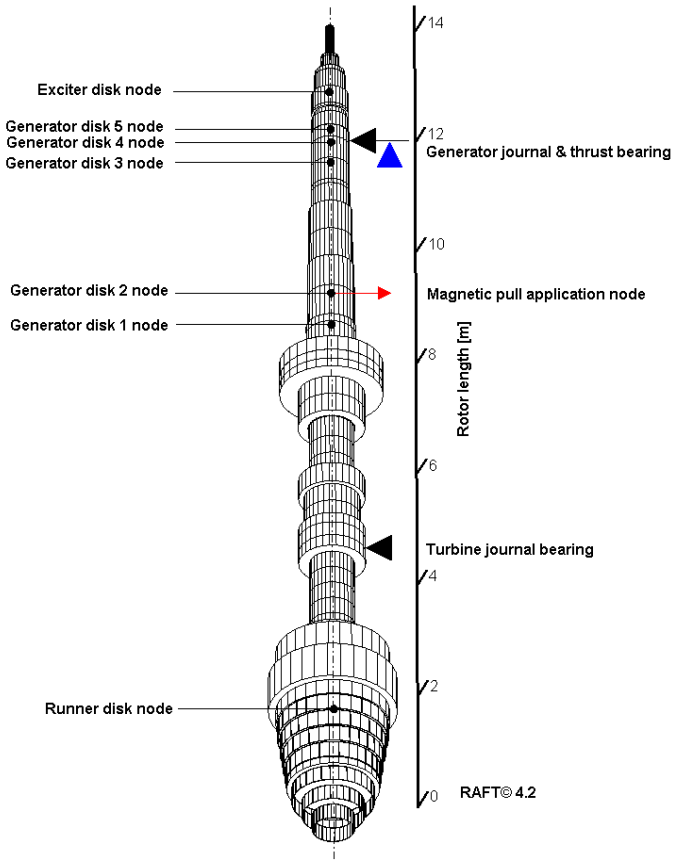

Figure 3. Sketch of the FEM.

(a)

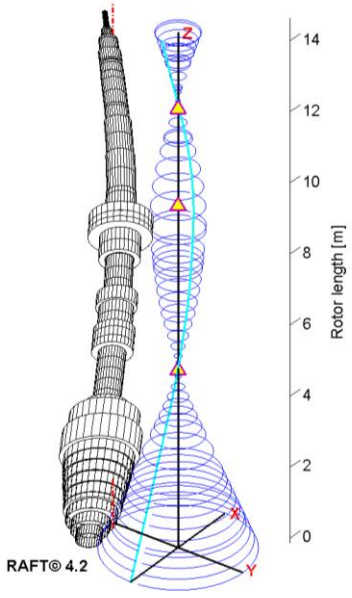

(b)

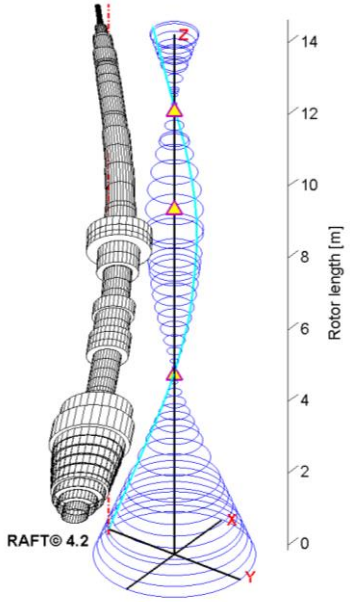

Figure 4. First bending mode affecting the runner: (a) backward mode with natural frequency of 6.0 Hz, (b) forward mode at 6.2 Hz.

(a) (b)

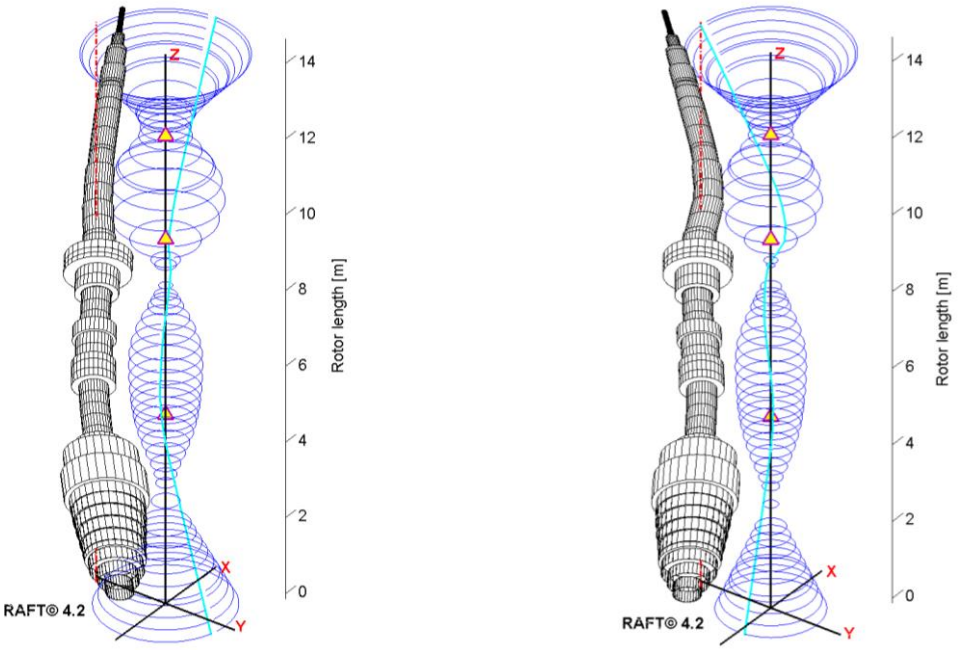

Figure 5. Second bending mode affecting the runner: (a) backward mode with natural frequency of 15.5 Hz, (b) forward mode at 19.5 Hz.

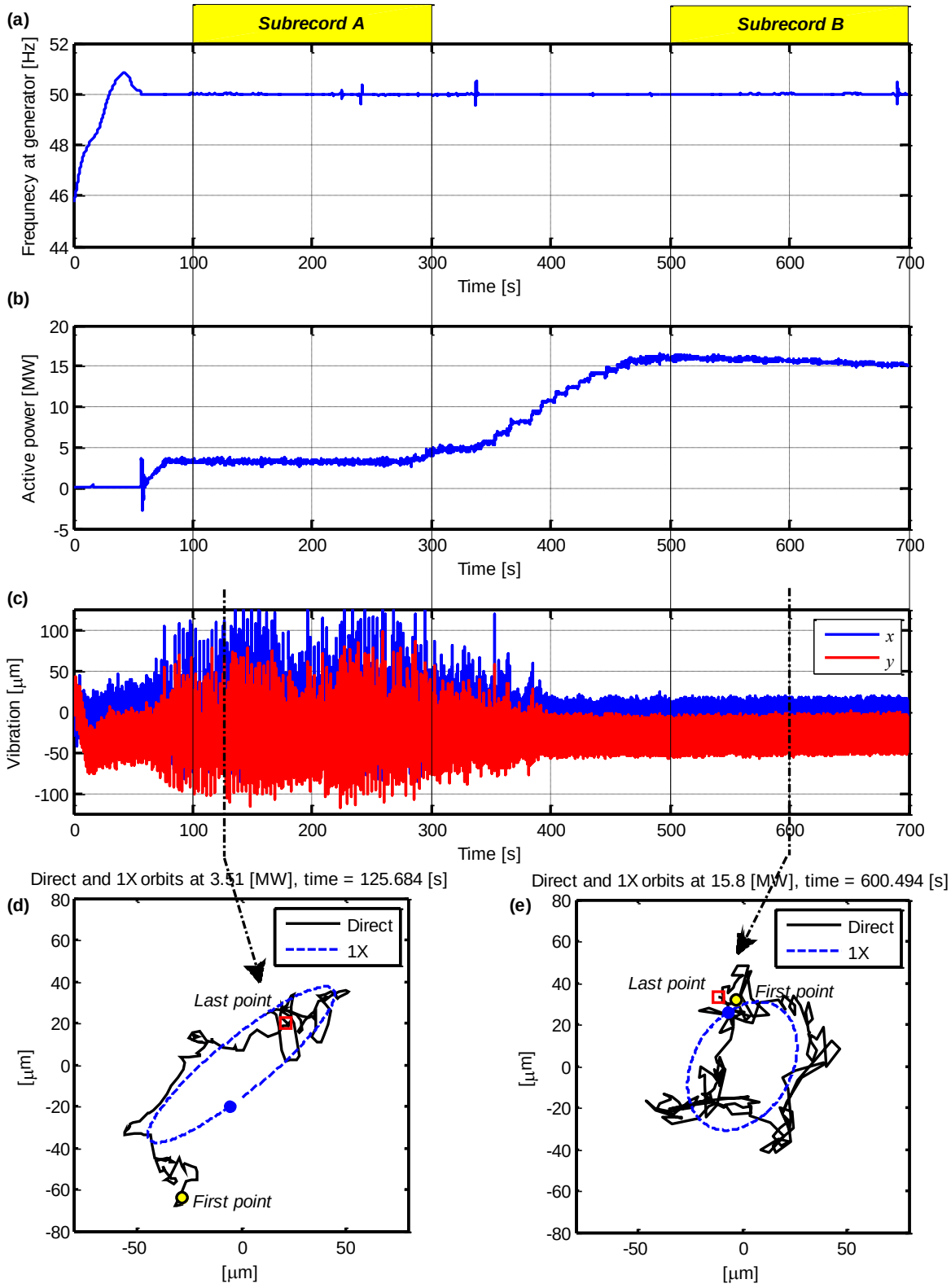

Figure 6. Measurements during start-up: (a) electric instantaneous frequency, obtained by processing a tachometer signal: (b) instantaneous power output, (c) rotor vibrations in two orthogonal directions of the shaft section, measured by proximitors installed in the stator at the turbine end of the shaft, (d) rotor direct and 1X orbits at about 3MW, (e) rotor direct and 1X orbits at about 16MW.

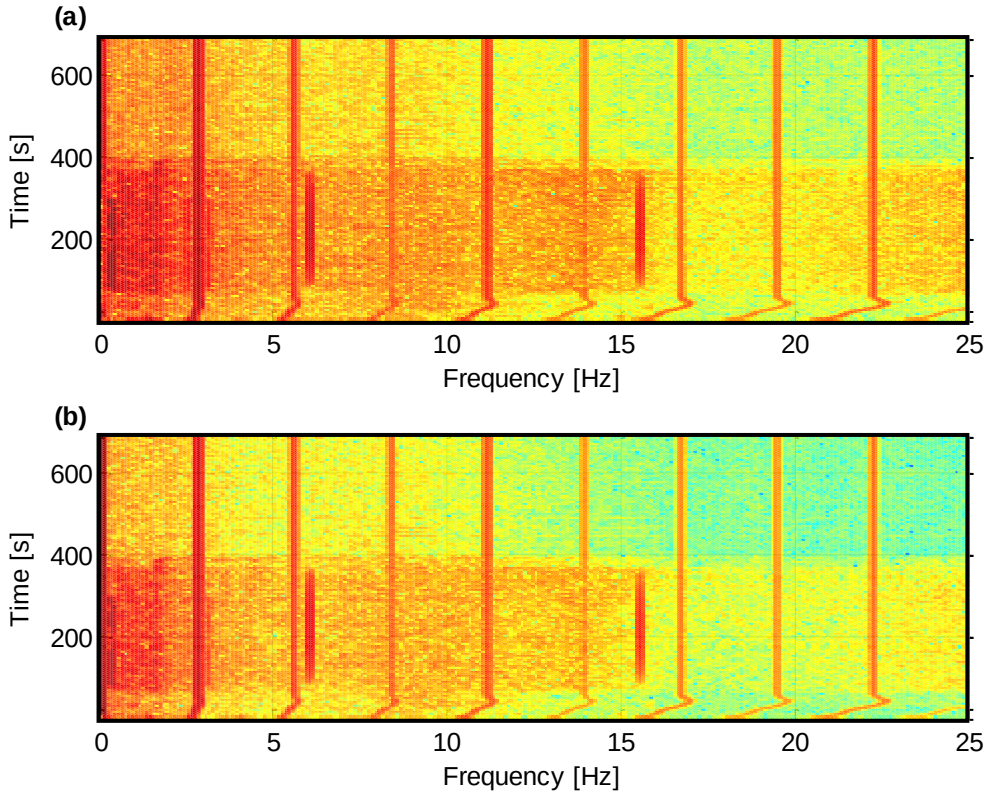

Figure 7. Raw spectrograms of the vibration signals: (a) *x* direction; (b) *y* direction. All diagrams have log scale z axis.

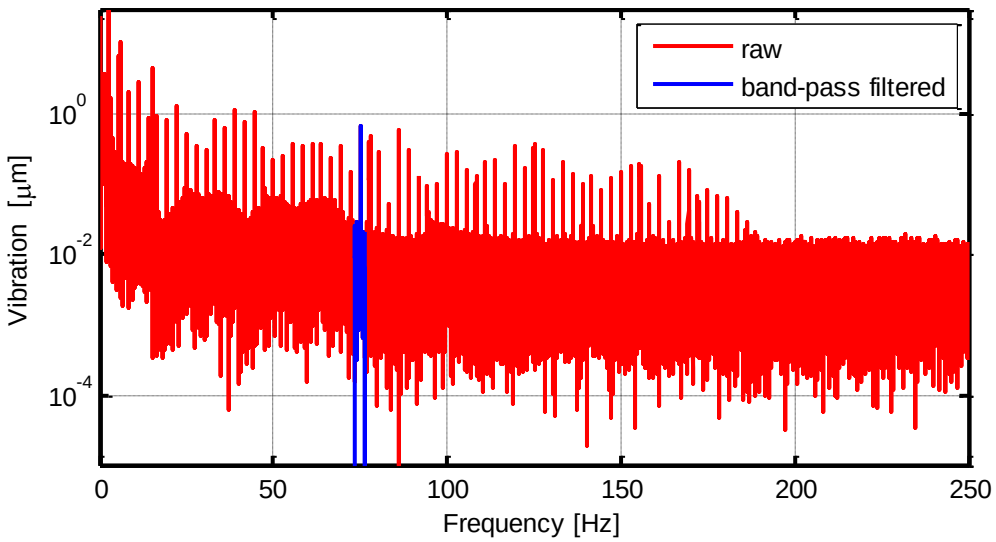

Figure 8. Extraction of an artificial tacho signal from the vibration signal itself (*x* vibration) by band pass filtering in the spectral domain.

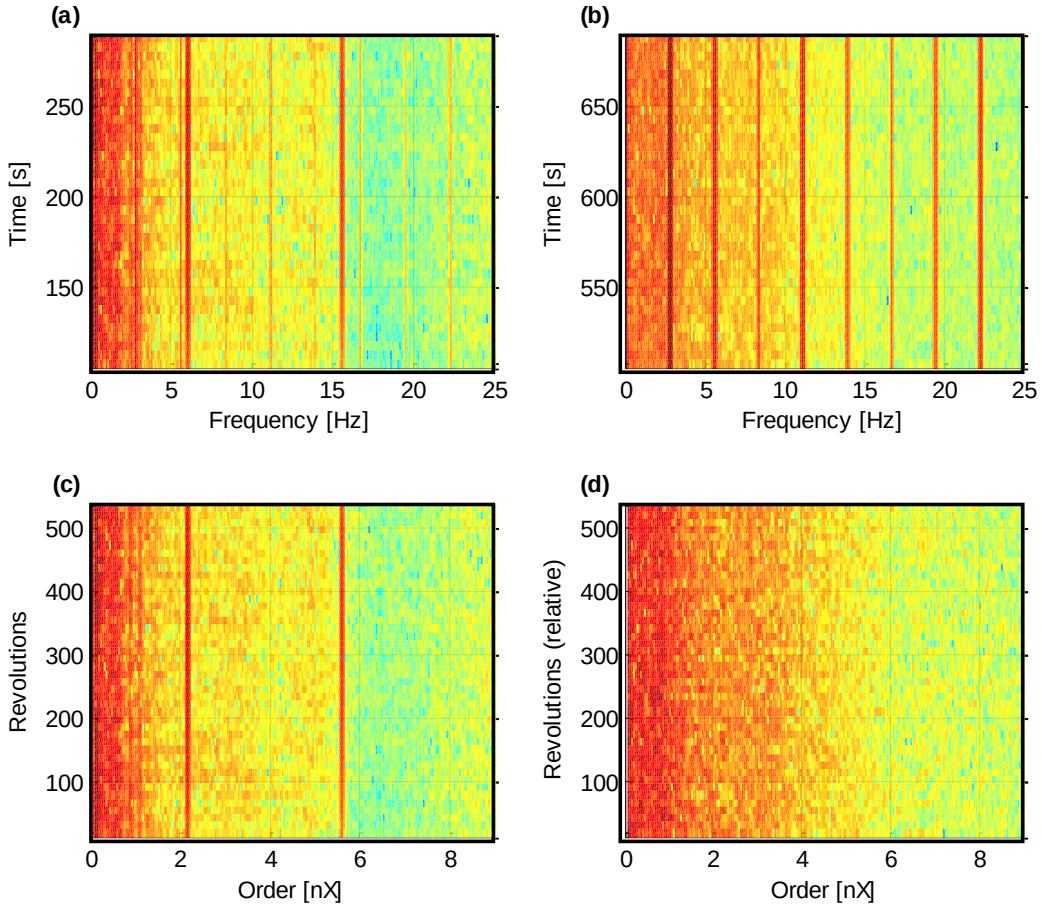

Figure 9. Removal of synchronous components in the *x*-vibration signal: (a) spectrogram of the subrecord A before order tracking, (b) spectrogram of subrecord B before order tracking, (c) spectrogram of the residual of subrecord A after COT/SA, (d) spectrogram of the residual of subrecord B after COT/SA. All diagrams have log scale z axis.

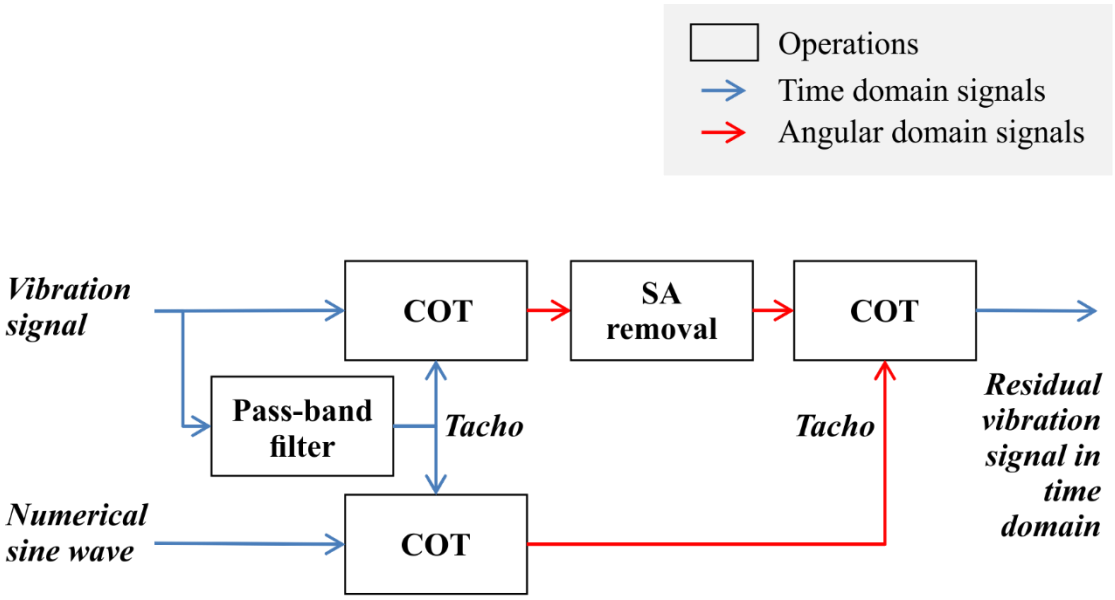

Figure 10. Procedure to obtain clean vibration signals in time domain, without additional experimental signals.

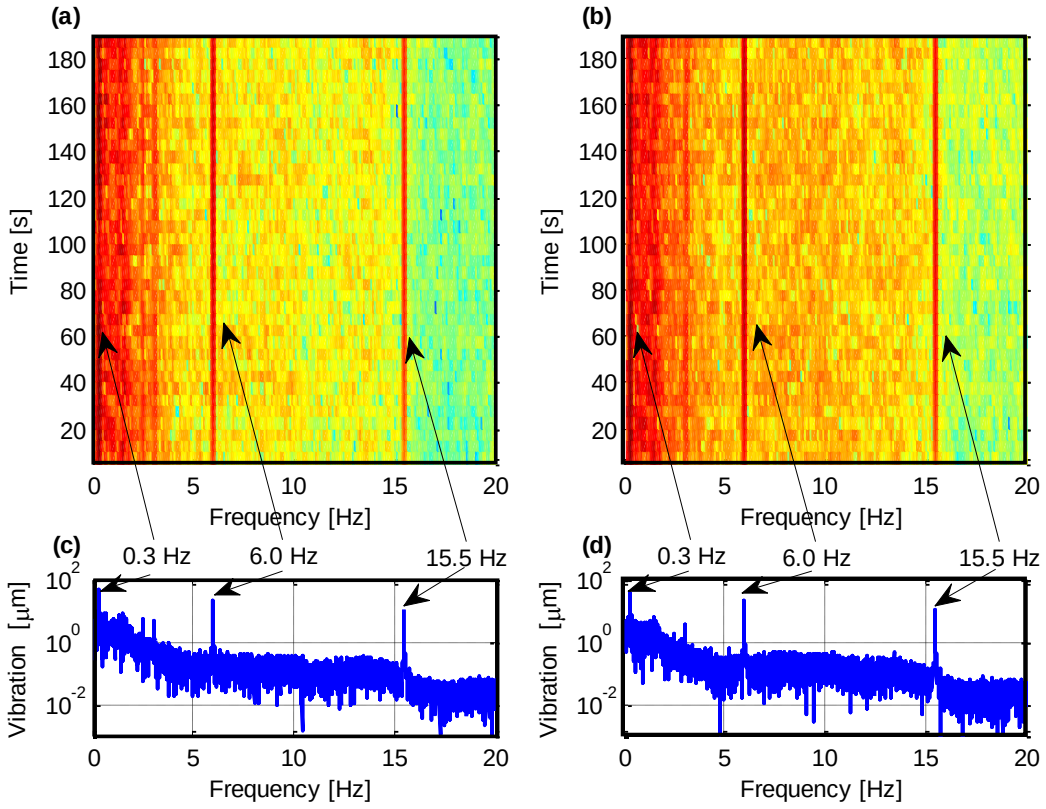

Figure 11. Residual of the subrecord A: (a) spectrogram *x* direction; (b) spectrogram *y* direction; (c) spectrum *x* direction; (d) spectrum *y* direction. All diagrams have log scale z axis.

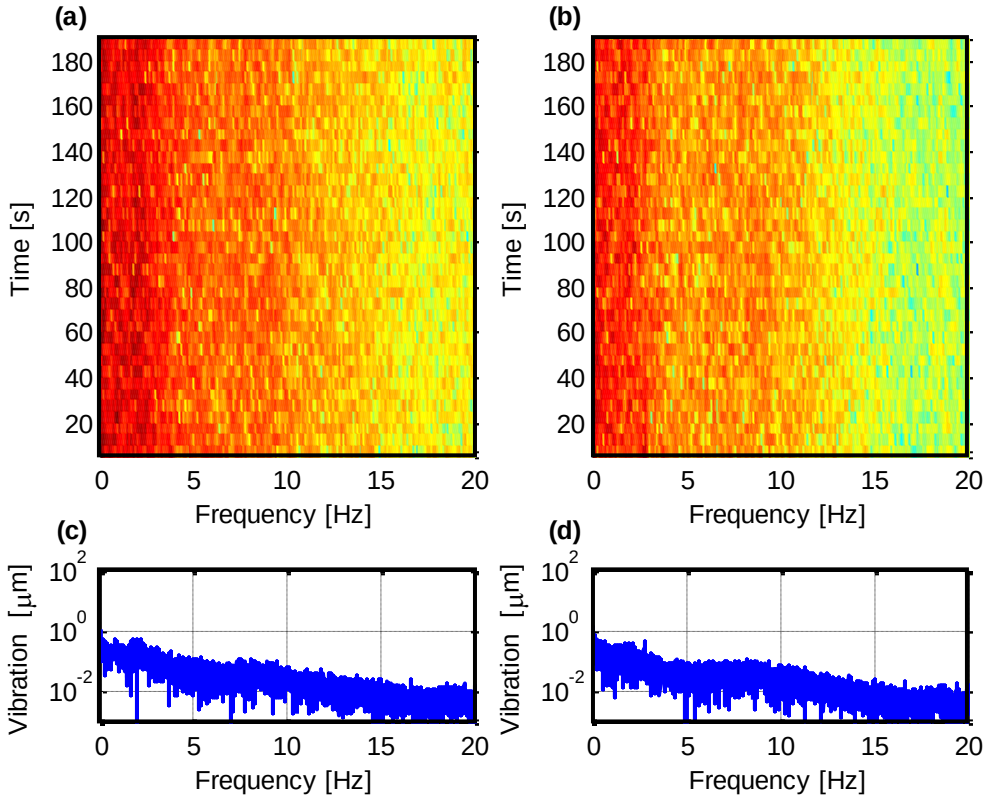

Figure 12. Residual of the subrecord B: (a) spectrogram *x* direction; (b) spectrogram *y* direction; (c) spectrum *x* direction; (d) spectrum *y* direction. All diagrams have log scale z axis.

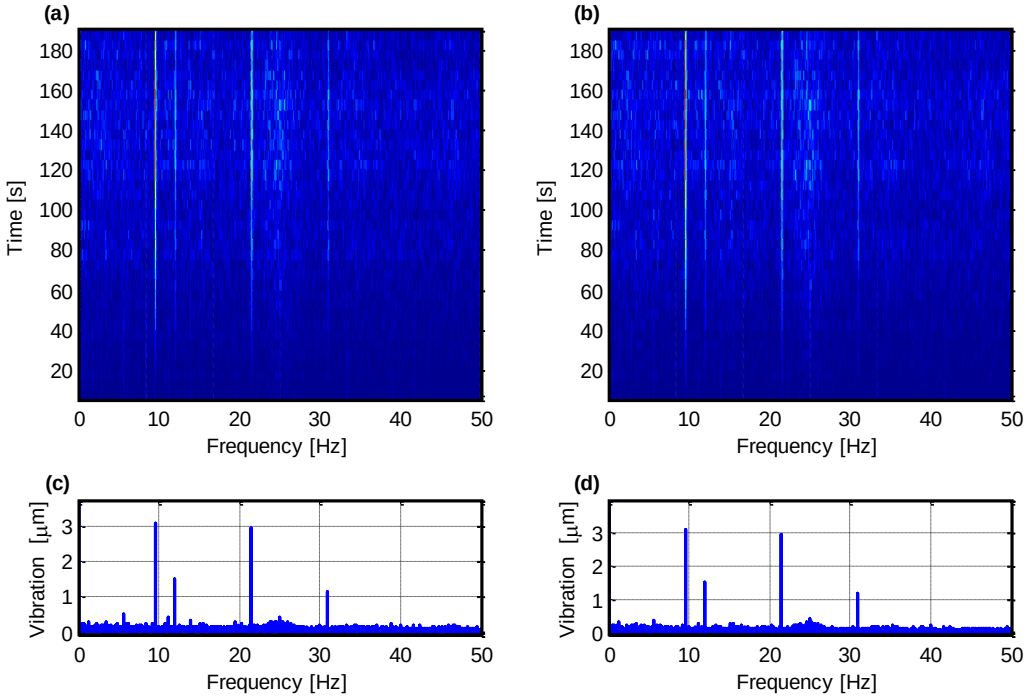

Figure 13. Envelope analysis for the subrecord A: (a) envelope spectrogram *x* direction; (b) envelope spectrogram *y* direction; (c) envelope spectrum *x* direction; (d) envelope spectrum *y* direction. All diagrams in linear scale.

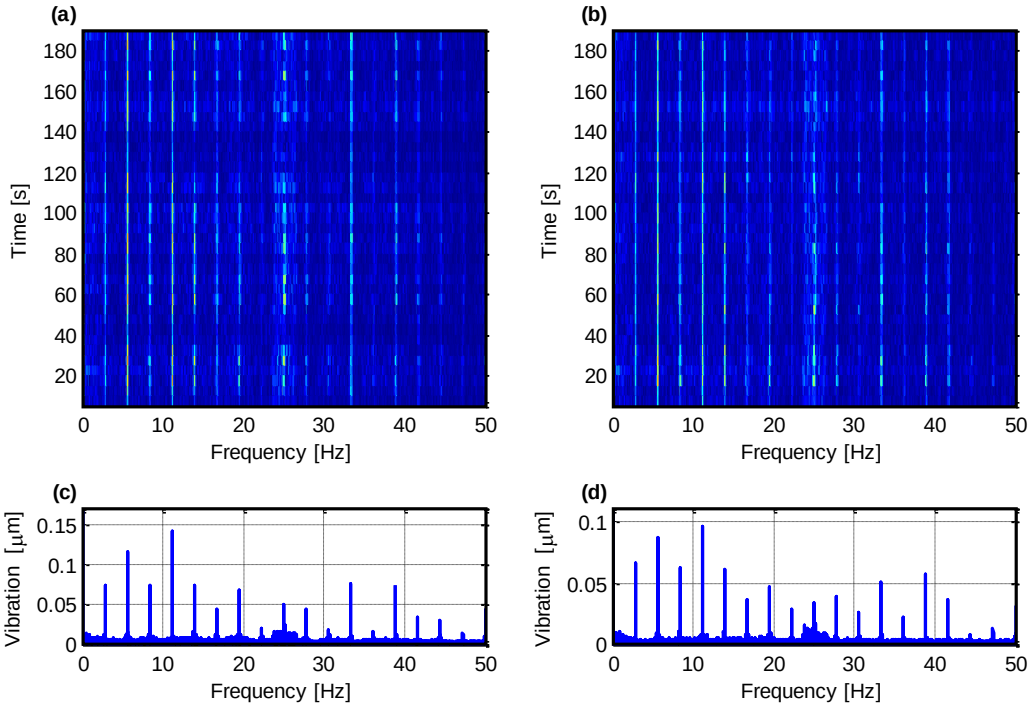

Figure 14. Envelope analysis for the subrecord B: (a) envelope spectrogram *x* direction; (b) envelope spectrogram *y* direction; (c) envelope spectrum *x* direction; (d) envelope spectrum *y* direction. All diagrams in linear scale.

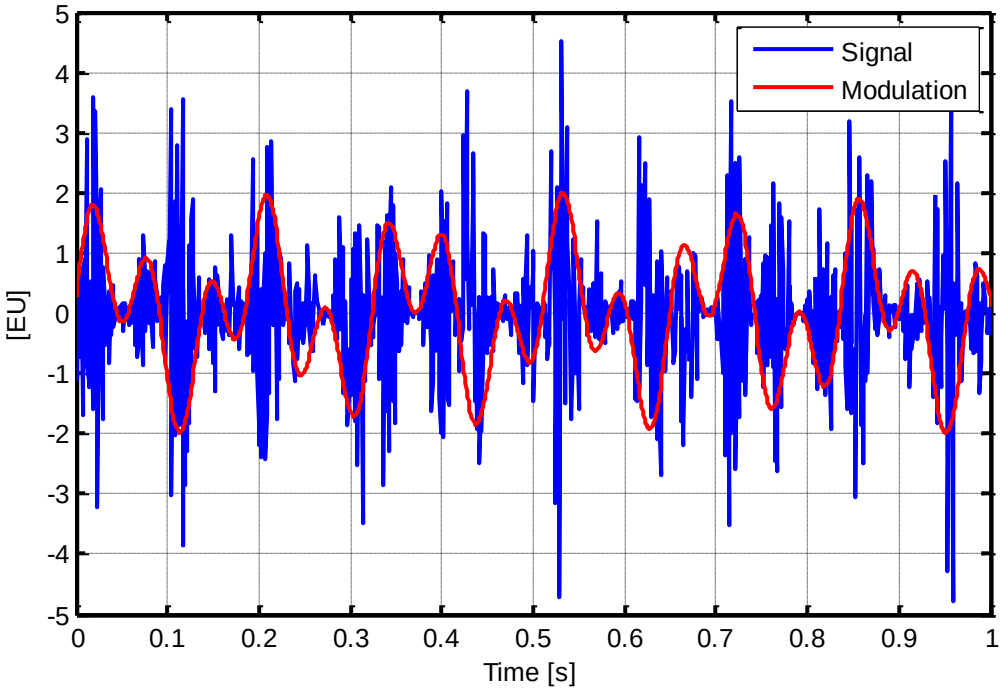

Figure 15. First second of the artificially generated signal obtained modulating white noise with a biharmonic signal.

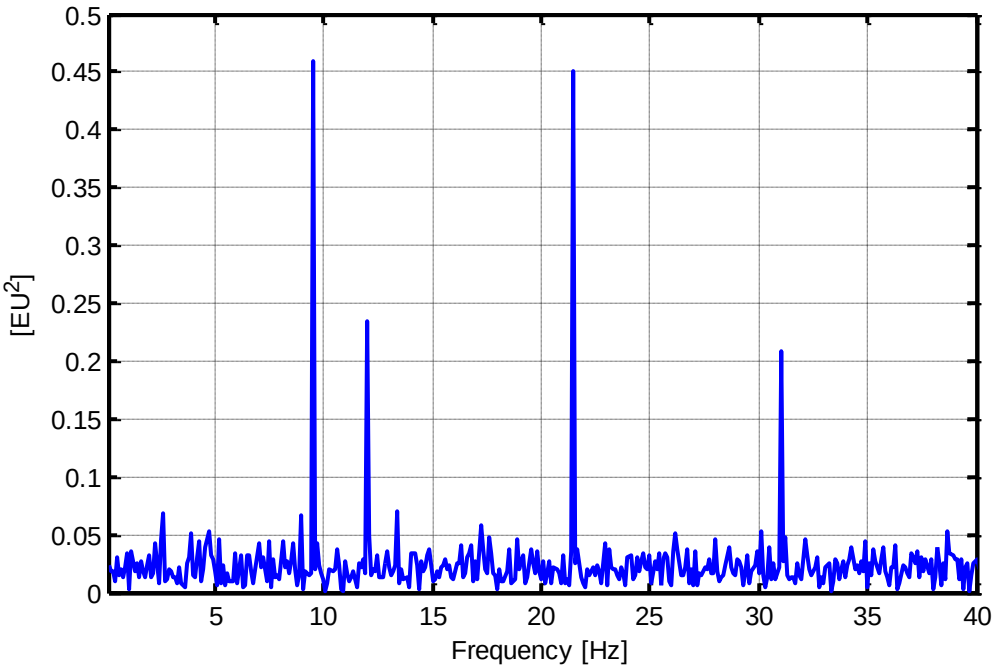

Figure 16. Envelope spectrum of the numerical simulation of a CS2 signal due to a biharmonic modulation of white noise.

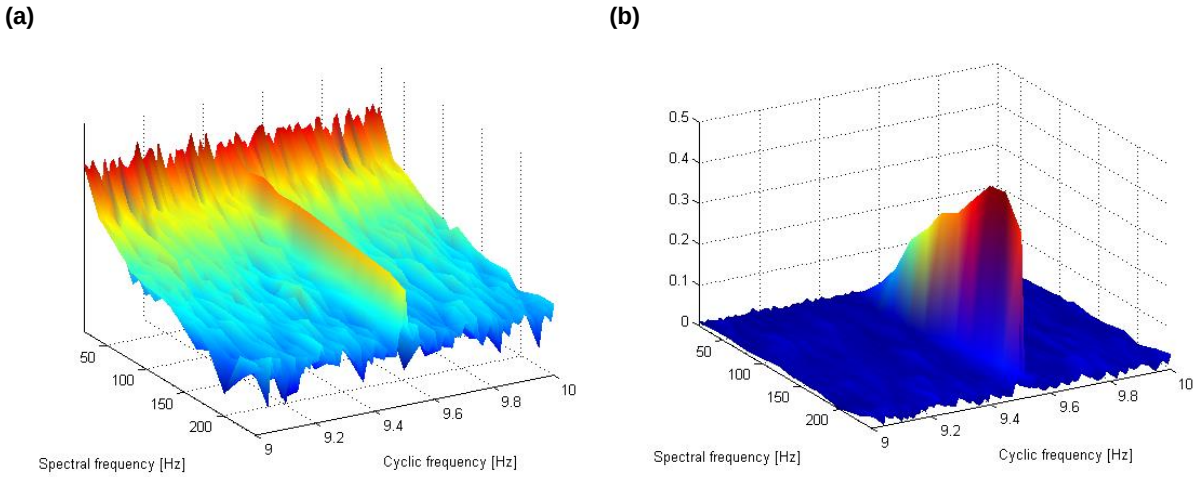

Figure 17. Neighbourhood of 9.5 Hz, subrecord A: (a) cyclic correlation, Log z-axis scale; (b) cyclic coherence.

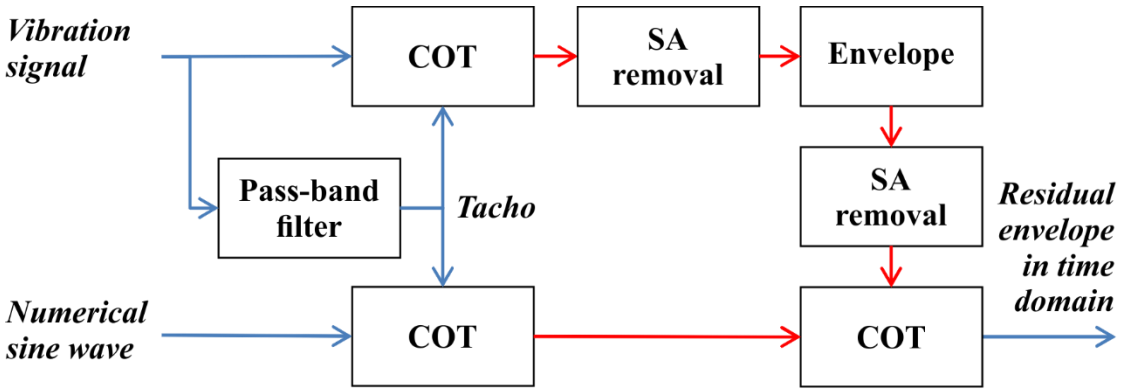

Figure 18. Procedure to obtain clean envelope signals in time domain, without additional experimental signals.

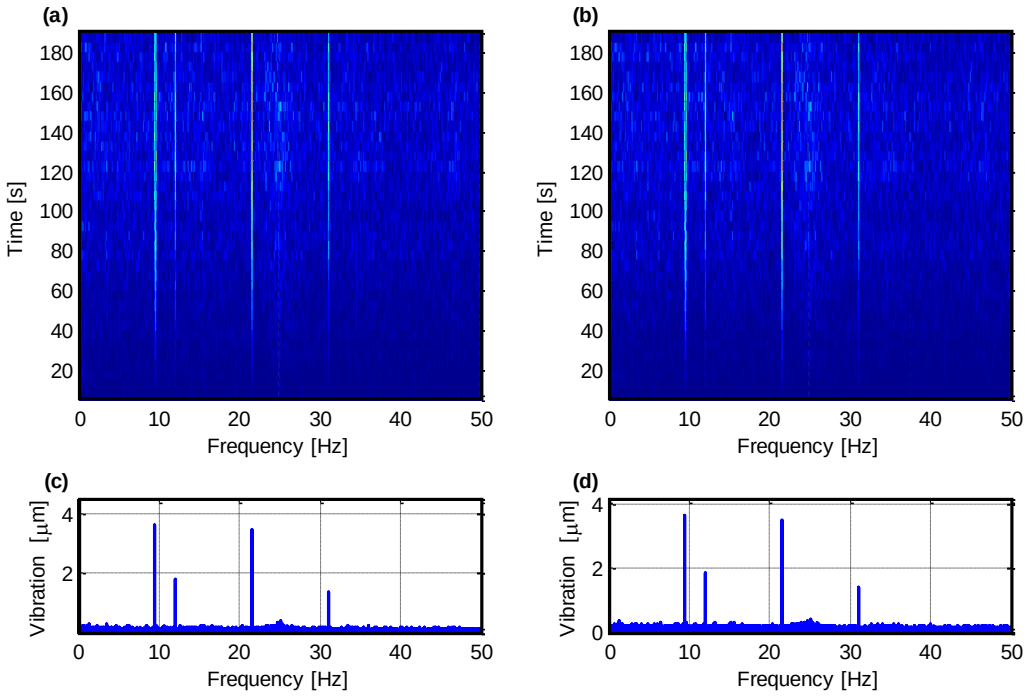

Figure 19. Envelope analysis for the subrecord A after removal of synchronous CS2 components: (a) envelope spectrogram *x* direction; (b) envelope spectrogram *y* direction; (c) envelope spectrum *x* direction; (d) envelope spectrum *y* direction.

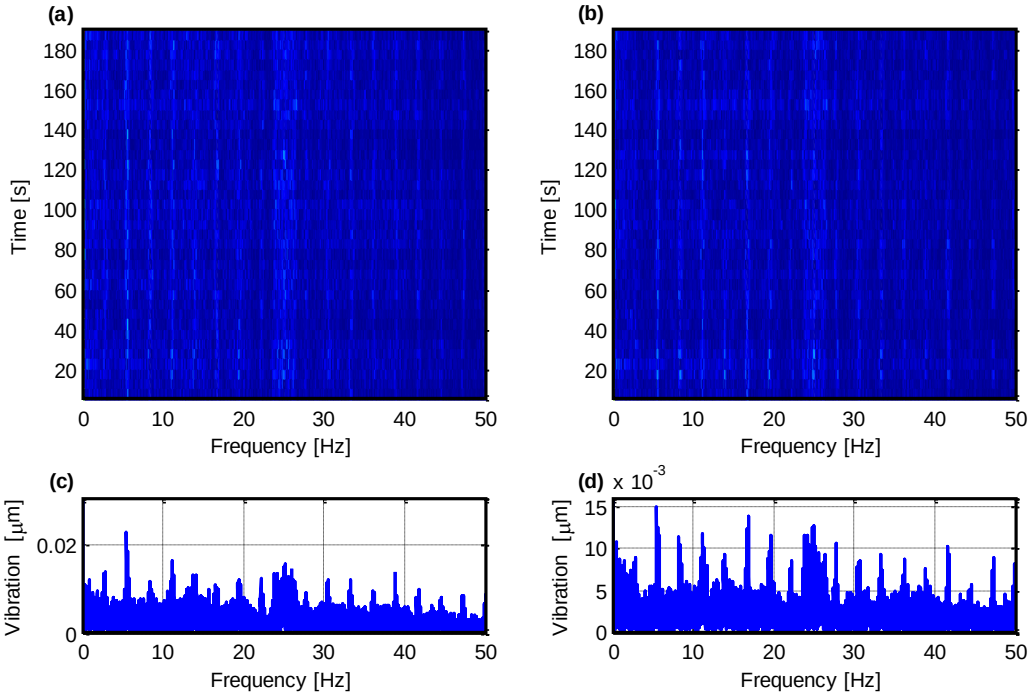

Figure 20. Envelope analysis for the subrecord B after removal of synchronous CS2 components: (a) envelope spectrogram *x* direction; (b) envelope spectrogram *y* direction; (c) envelope spectrum *x* direction; (d) envelope spectrum *y* direction.